Title

Kinetic and thermodynamic analysis of high-temperature CO2 corrosion of carbon steel in simulated geothermal NaCl fluids

Authors

Mundhenk, N
Carrero, S
Knauss, KG
et al.

Publication Date

2020

DOI

10.1016/j.corsci.2020.108597

Corrosion Science 171 (2020) 108597

Contents lists available at ScienceDirect

Corrosion Science

journal homepage: www.elsevier.com/locate/corsci

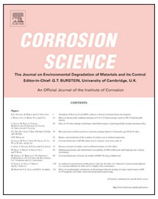

Kinetic and thermodynamic analysis of high-temperature CO_2 corrosion of carbon steel in simulated geothermal NaCl fluids

N. Mundhenk[a,*], S. Carrero[a,b], K.G. Knauss[a], R. Wonneberger[c], A. Undisz[c], Y. Wu[a]

[a] Earth & Environmental Sciences Area, Lawrence Berkeley National Laboratory, Berkeley, CA, 94720, United States
[b] University of California, Berkeley, CA, 94720, United States
[c] Otto Schott Institute of Materials Research, Chair of Metallic Materials, Friedrich-Schiller-University, 07743, Jena, Germany

ARTICLE INFO

Keywords:
CO_2corrosion
Carbon steel
Thermodynamics
Kinetics
TEM

ABSTRACT

We discuss kinetic and thermodynamic aspects of carbon steel corrosion in CO_2-containing NaCl fluids up to 240 °C. Crystalline nm-thick Fe-oxide films only form at 160 °C and 240 °C providing instantaneous and moderate corrosion protection. The absence of Fe-oxide at 80 °C results in high initial corrosion rates until a moderately protective, but thick and porous, $FeCO_3$ film forms. From the metal/film interface it grows inwards by replacing ferrite with $FeCO_3$. TEM reveals a precursory, likely hydrated and chloride-containing, phase that predates $FeCO_3$ formation. Thermodynamic predictions agree well with experimental results in that Fe-oxide formation is favored over $FeCO_3$ towards higher temperatures.

1. Introduction

Geothermal fluids are inevitably corrosive towards engineering metals, arising from the combination of high temperatures and the presence of corrosive species, e.g. chloride ions and/or dissolved CO_2 [1,2]. Such fluids are encountered not only in geothermal operation, but also in CO_2 sequestration, nuclear waste disposal, and hydrocarbon exploration, where oil and gas is increasingly produced from deeper reservoirs. The integrity of subsurface structures is therefore a main concern in geotechnical applications. Material degradation and failure might lead to contamination of aquifers or to significant downtime periods in operation. Another concern arises from the observation that precipitates on corroding metal surfaces can accumulate significant amounts of toxic substances and radionuclides [3]. In geothermal binary cycle power plants, such scales not only decrease the efficiency of the heat exchange but also require extensive cleaning operations with strict regulations on safety and radioprotection.

Numerous engineering materials have been tested in both simulated and in-situ geothermal environments [2,4–10]. These include materials for well casings, surface pipes, heat exchangers, turbines, including carbon steels, stainless steels, non-ferrous metals, and other non-metallic materials. The corrosion-relevant physicochemical conditions have been site-specifically monitored and discussed globally. Various factors have been found to significantly impact the corrosion rate of engineering materials (e.g. salinity, chloride concentration, dissolved gas chemistry, temperature, microbial activity, flow rate, microstructure and composition, and pH) among which temperature plays a key role in many corrosion systems. It is the main driver that accelerates all the processes involved: electrochemical, chemical, and transport [11]. Another important factor is time and instantaneous corrosion rates have been found to vary over orders of magnitude between initial (Fe_3C-catalyzed) and steady-state corrosion rates [12,13]. This wealth of influencing and often time-variant factors makes a comprehensive assessment of material stabilities technically impossible. Rather subtle changes in corrosion mechanisms are easily overlooked by studying an array of influencing factors.

Dissolved or gaseous CO_2 is ubiquitous in geothermal fluids. CO_2 corrosion (“sweet corrosion”), mainly in the context of hydrocarbon exploration and transportation, has been discussed extensively by many authors [2,11–17]. CO_2 can have a corrosion-enhancing or corrosion-inhibiting impact on the corrosion rate. For instance, CO_2 is known to electrochemically enhance corrosion rates by lowering the pH and introducing additional reducible species (e.g. H_2CO_3, HCO_3^-). On the other hand these species can react with anodically-released iron cations to form corrosion films that, depending on an array of factors, potentially have protective properties [11,18]. The kinetics of corrosion is strongly impacted by the formation and properties of corrosion films. Which phases will form (e.g. oxides, carbonates) not only depends on the availability of species in the fluid and the temperature, but on the degree of oversaturation and the relative kinetics of nucleation and

---

[*] Corresponding author.
E-mail address: nmundhenk@lbl.gov (N. Mundhenk).

https://doi.org/10.1016/j.corsci.2020.108597
Received 22 August 2019; Received in revised form 9 March 2020; Accepted 10 March 2020

crystal growth. It is therefore not uncommon for a metastable or amorphous phase to form preferential to a thermodynamically stable phase [19–21]. In addition, kinetic effects on film growth, as well as the relative kinetics of nucleation and crystal growth for the individual phases, are important and can strongly alter thermodynamically predicted outcomes.

Despite its overarching importance, there are only a very limited number of studies that focus solely on temperature exceeding 160 °C, particularly in the presence of CO_2. For instance, Posey et al. found a linear relationship in deaerated NaCl solution up to 250 °C [9]. Kurata et al. also found increasing corrosion rates for various materials as temperature increased in the range between 150 °C and 300 °C [10]. The presence of CO_2, however, complicates the matter and existing research is very ambiguous as to whether corrosion intensifies as temperature increases. This is mainly due to an incomplete understanding of corrosion films and their structural properties. For instance, corrosion films can be intrinsically protective or facilitate passivation beneath a moderately protective film [11,14]. The lack of research on this particular topic is also due to the inherent difficulty running well-controlled electrochemical experiments under high-temperature/high-pressure conditions. In this study we use electrochemical and surface analytical techniques to obtain a better understanding of carbon steel corrosion at geothermally-relevant temperatures. A highly saline and CO_2-containing fluid mimicking a natural geothermal fluid is used for the flow-through experiments. Thermodynamic calculations were carried out, providing a basis for discussing the results from the kinetic study.

2. Experimental

The experiments were conducted at 160 and 240 °C for variable durations (up to 4 days) in an all-titanium mixed flow reactor (Parr Instruments) with a volumetric capacity of 300 ml. It was constantly stirred at 500 rpm. The flow rate is held constant at 0.5 ml/min so that the reactor volume is exchanged every 10 h. A pressure of 70 ± 4 bar was maintained over the course of the experiment to prevent CO_2 degassing. It took about 1–1.5 hours to reach the target temperature and pressure. During that time the samples were already immersed in corrosive solution.

Corrosion experiments were conducted with 1045 carbon steel samples with the following composition [wt.%]: C 0.48, Mn 0.75, Fe balance. 1045 is similar to API grade P110 (C 0.41, Mn 0.34, Fe balance), which is often used for pipeline applications. The high carbon content leads to a ferritic-pearlitic microstructure, in which pearlite is a two-phase mixture consisting of alternating plates of ferrite and cementite (Fe_3C). For each experiment two cylindrical samples were placed in the reactor: one working electrode ($2.63\ cm^2$) connected to a potentiostat and one sample ($2.57\ cm^2$) for ex-situ analysis. Before each experiment the samples were sequentially polished up to 1200 grit, rinsed with water, degreased in acetone, and dried.

The corrosive fluid contained 2 M NaCl and 40 mM $NaHCO_3$. It was equilibrated for at least 24 h in a 4 L titanium vessel at 10 bar pCO_2 (research-grade). Deaeration was achieved by adding the salts under N_2 atmosphere to deionized water (18.2 MΩ cm) that had been boiled vigorously for 15 min. Using PhreeqC with the preeqc.dat database we calculated a solution pH of ~5.1 (at 25 °C) and a total dissolved carbon concentration of $0.2723\ mol\ kg^{-1}$ in the starting fluid [22]. Under in-situ conditions $CO_{2(aq)}$ is the species present in the highest concentration (~85 mol% of the total dissolved carbon). The pH for the different temperatures was calculated to be 4.8, 5.3, and 6 at 80, 160, and 240 °C, respectively. Geochemist's Workbench was used for the generation of pH-temperature plots using the thermo.com.V8.R6 + .dat database [23].

Electrochemical experiments were conducted with a standard three-electrode setup with the 1045 carbon steel sample as the working electrode, a Pt mesh counter electrode, and an external Ag/AgCl (0.1 M KCl) reference electrode purchased from Corr Instruments, LLC. All electrochemical potentials reported in this study are referenced to the standard hydrogen electrode (SHE). The pressurized shaft around the sensing element was cooled to 15 − 20 °C by a recirculating chiller. A Princeton Applied Research potentiostat (PARSTAT 4000A) was used for data acquisition. During the experiment the corrosion potential E_{corr}, and the linear polarization resistance (R_p) were measured continuously. R_p tests were conducted by polarizing from −10 to 10 mV vs. open circuit potential (OCP) with a scan rate of $0.25\ mV\ s^{-1}$. Before terminating the experiment after 1 and 4 days, a potentiodynamic polarization (PDP) curve was measured by polarizing the sample from −250 mV to +500 mV (vs. OCP).

A scanning electron microscope (SEM; Zeiss Evo LS10) equipped with an energy dispersive X-ray (EDX) detector was used for structural and compositional analysis of the corrosion films (acceleration voltage 15 kV). XRD measurements were conducted with a Siemens D500 diffractometer using Cu kα 1 (λkα1 = 1.5406 Å) and kα 2 (λkα2 = 1.5444 Å) radiation. Data were collected from 2 to 90°2θ with a 0.02°2θ step-size and count times of 2 s per step. The diffraction pattern was collected on a diffractometer in Bragg-Brentano geometry, equipped with a theta-theta goniometer with a rotating sample holder. The diffraction patterns were analyzed using the software Match extended with the PDF (powder diffraction file) mineral database.

Transmission electron microscopy (TEM), high-resolution transmission electron microscopy (HRTEM) and scanning transmission electron microscopy (STEM) were carried out using a JEOL NEOARM 200F operating at 200 kV. The device was equipped with a cold field emission gun, a 4k x 4k Gatan OneView CCD-camera and two windowless silicon drift detectors for energy dispersive X-ray spectroscopy with a total detector area of $200 mm^2$ (JEOL Centurio). Samples for TEM were prepared using a focused ion beam system (Helios NanoLab 600i, FEI). In case of the 80 °C sample the corrosion film was removed by grinding using 1200 grit until parts of the alloy surface got visible for a targeted preparation of the corrosion film/metal interface.

3. Results and discussion

3.1. Study of corrosion kinetics

3.1.1. Potentiodynamic polarization (PDP)

Fig. 1a gives the PDP curves that have been measured at 160 °C and 240 °C after 1 and 4 days, respectively. Kinetic information from PDP measurements can typically be extracted by using the Tafel extrapolation method in which the corrosion current j_{corr} can be extracted by extrapolation of the Tafel lines to the corrosion potential [24]. However, the applicability of this method for our experiments is limited due to the absence of anodic Tafel behavior at both temperatures. This suggests the existence of a dissolution reaction in conjunction with a film-forming reaction. Nonetheless, the lower current densities over a wide range of anodic potentials indicate a lower corrosion rate at 160 °C. This is qualitatively consistent with the anodic polarization results from Heusler et al. [25]. They reported an anodic current density approx. one order of magnitude higher at 250 °C than at 150 °C, albeit in the absence of CO_2. By extrapolating the measurements at different anodic overpotentials to the OCP, they found a maximum rate constant between 230 °C and 250 °C.

The cathodic branches reveal a minor influence of temperature and immersion time on the cathodic reaction, which under these conditions is the hydrogen evolution reaction (HER) by reduction of the H^+ part of the H_3O^+, H_2O; and HCO_3^- [16]. Previous research has shown that Fe_3C, which is a metallic conductor and has a low hydrogen overvoltage, provides a good surface for the cathodic HER. This lead to the conclusion that galvanic coupling between Fe_3C and ferrite accelerates corrosion substantially by preferentially dissolving the ferrite [26].

The anodic branches are more dependent on temperature and show peaks and plateaus, indicating the occurrence of anodic interfacial

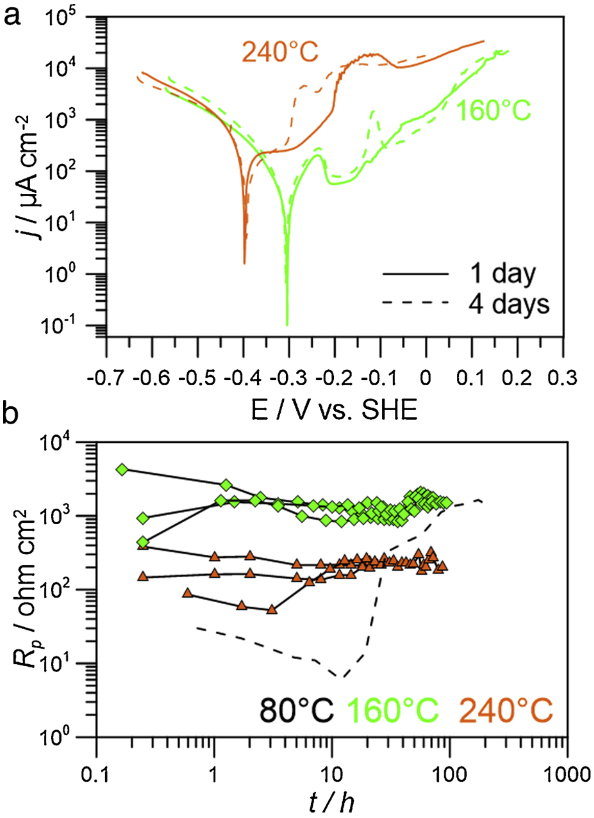

Fig. 1. (a) Potentiodynamic polarization curves for 160 °C and 240 °C measured after 24 h (scan rate: 1 mV s^{-1}); (b) Linear polarization resistance (R_p) versus time (80 °C data are from Mundhenk et al. [12].

reactions. Minor discrepancies can typically be found in the anodic branches when comparing the 1 and the 4 days experiments, showing that steady-state conditions are achieved relatively early during the experiments. At any given anodic potential the current density is higher at 240 °C than at 160 °C. For both temperatures, however, the observed plateau currents are too high to be considered as being in the true passive state. The terms pseudo- or semi-passive are typically used to describe such observations [16]. At 160 °C an active-passive transition is observed with a current peak of 200 − 250 μA cm^{-1} at −232 mV before the current drops to 60–80 μA cm^{-1}. Another oxidation reaction (4 days sample) occurs at −115 mV and is likely attributed to an oxidation reaction within the film (Fe^{2+} to Fe^{3+}). At 240 °C an active-passive transition is not observed and the corrosion potential lies in a plateau region that is characterized by a current density of 120 − 240 μA cm^{-1}. A significant increase in current density occurs at a potential of approx. −192 mV (1 day sample) and −300 mV (4 days sample), respectively. The observed differences after 1 and 4 days underscore that the metal surface is a highly dynamic local environment.

3.1.2. *Linear polarization resistance (R_p)*

Fig. 1b shows that the R_p at 160 °C and 240 °C is relatively constant over the course of several days. For each temperature three measurements are given that show good agreement after ~10 h of immersion. R_p is significantly higher for 160 °C (~1500 Ω cm^2) than for 240 °C (~200 Ω cm^2).

At 160 °C the R_p rises to slightly higher values after ~40 h of immersion. An increase cannot be observed for the 240 °C experiments. This is in disagreement with the results reported in Park and Macdonald [27] for similar temperatures, whose data show a substantial decrease in R_p caused by autocatalytic corrosion due to the development of a low-pH electrolyte within the pores by cation hydrolysis. This apparent disagreement can be resolved by considering the buffering effect of the electrolyte which prevents strong local acidification.

The observed behavior at 160 °C and 240 °C is in stark contrast to what we observed at 80 °C, where corrosion appears to proceed in the absence of a protective Fe-oxide film. R_p was found to be strongly variable with time, which is indicated by the dashed line in Fig. 1b. Low R_p values in the initial stage of the experiments suggest that corrosion is catalytically enhanced and instantaneous corrosion rates of up to 30 cm y^{-1} are observed [12]. Similar results have been found by Farelas et al. [13] and have been attributed to the selective dissolution of the ferrite component within the steel microstructure. The carbon content, which determines the volume fraction of the Fe_3C component in the microstructure, has been shown to be critical to explain due to its metallic conductivity and participation as a cathodic surface. After approx. 20 h at 80 °C, R_p suddenly increases and reaches values around 1500 Ω cm^2. This marks the point in time when the electrochemically active sites are covered with $FeCO_3$ and the corrosion rate becomes controlled by diffusion through a porous and relatively thick $FeCO_3$ film. The steady-state R_p measured at 80 °C is similar to that at 160 °C which suggests a comparable steady-state corrosion rate.

3.1.3. *Corrosion potential (E_{corr}) measurements*

Fig. 2 shows the E_{corr} over the course of 4 days beginning at the point when the target temperature and pressure were reached (approx. 1 h for 160 °C and 1.5 h for 240 °C). At both temperatures E_{corr} is increasing over the course of the experiment until steady-state conditions appear to be achieved after ~48 h. This is consistent with data reported by Park & Macdonald [27] who also report a moderate increase of the E_{corr} in the very early stage of corrosion. The low variation with time indicates that steady-state conditions are achieved and that both, the anodic and the cathodic reaction proceed at constant rates. Minor fluctuations are understood as being due to changes in the area ratios between anode and cathode. The steady-state E_{corr} is slightly higher at 160 °C compared to 240 °C. Increasing corrosion potentials typically indicate either a disproportionate retardation of the anodic reaction or an enhancement of the cathodic reaction. This either means that the cathodic reaction occurs faster at 240 °C or that the anodic reaction is faster at 160 °C. The latter seems less likely since no substantial difference in cathodic reaction rate at 160 and 240 °C was observed in PDP measurements (Fig. 1a).

At 80 °C E_{corr} increases by almost 250 mV, leveling off at a value of ~ −220 mV after several days. This prolonged increase sets apart the experiments at 80 °C from the results obtained for 160 °C and 240 °C, respectively. As we will discuss later, this has strong implications for the formation and structure of the corrosion film.

3.2. *Corrosion film composition, structure and passivating properties*

Temperature was found to be a major factor in determining the

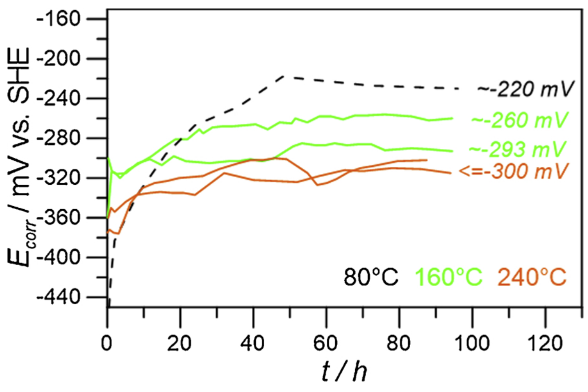

Fig. 2. Corrosion potential (E_{corr}) as a function of time; the data for 80 °C is from Mundhenk et al. [12].

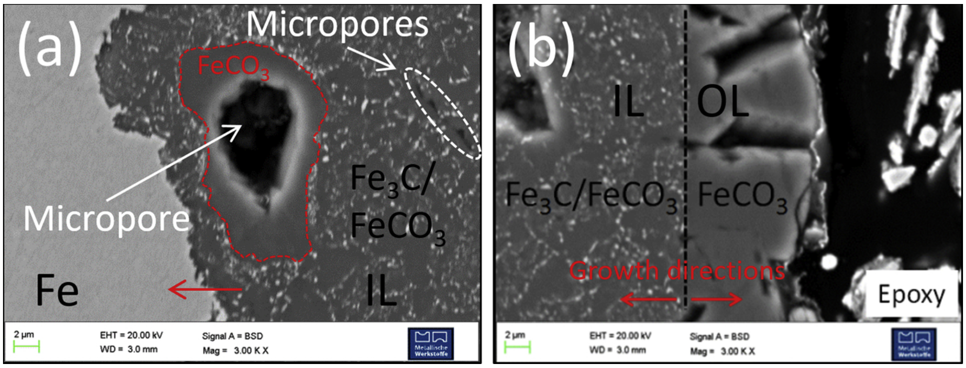

Fig. 3. Cross-sectional SEM-BSD (backscatter diffraction) images of (a) the metal-film interface with micropore outlined (red dotted line) and (b) the outer $FeCO_3$ film and the buried $FeCO_3/Fe_3C$ film in which an undissolved part of the original microstructure (bright areas) is still visible; the red arrows indicate the growth directions. (For interpretation of the references to colour in this figure legend, the reader is referred to the web version of this article.)

structure and the composition of corrosion films. SEM, TEM, and XRD were used to characterize the corrosion product formed at 80, 160, and 240 °C. TEM analyses have been performed on an 80 °C and a 160 °C sample.

3.2.1. 80 °C corrosion film

After 10 days of immersion at 80 °C the sample is covered by a coherent corrosion film. The total thickness of the corrosion film can reach a thickness of > 100 µm, exceeding the volume that has been dissolved by corrosion. The corrosion film was found to be generally uniform in thickness and to have an internal duplex structure with an inner layer (IL) consisting of a mixture of $FeCO_3$ and Fe_3C and an outer layer (OL) consisting of $FeCO_3$. The IL and the OL are distinguished by their different microstructures. The Fe/IL and IL/OL interfaces are shown in Fig. 3a and b, respectively. The IL/OL interface represents the former steel interface (indicated by a dotted line). The buried IL appears to be very homogeneous across its entire thickness, which can reach up to 100 µm. The Fe_3C part within the IL appears bright in the SEM-BSD mode (Fig. 3b) and is an undissolved part of the original steel microstructure. The $FeCO_3$ crystals within the IL are typically less than micron-sized and intergrown with no visible grain boundaries. Noticeable is that the IL is interspersed with micropores aligned parallel some distance away from the metal surface (Fig. 3a). The OL is a ~10 µm thick coherent monolayer of $FeCO_3$ crystals. It has the morphology of a precipitate that grows without volume constraint, hence the larger crystal size. In addition, it contains significant porosity between individual crystals.

The formation of a thick $FeCO_3$-dominated duplex film eventually lowers the corrosion rate substantially (after approx. 24 h). However, at this point, a significant amount, approx. 100 µm of steel, has been dissolved and partially incorporated into the film. As indicated by the red arrow in Fig. 3a, the IL grows into the Fe.

The TEM images of the Fe/IL interface are shown in Fig. 4. They reveal that no additional passivating oxide layer was found at the M/IL interface Fig. 4a, b. This rules out the growth mechanism by which Fe-oxide forms underneath $FeCO_3$ due to a local high-pH environment, as reported in a similar study at 1 bar CO_2 partial pressure [14]. The internal structure of the IL alone is therefore considered decisive for its protective properties. Within the IL, micropores can be found (Figs. 3a, 4 a) and likely act as conduits allowing electrolyte to reach the metal surface. The existence of a continuous pore network is required for corrosion to proceed. In addition, microfractures in the vicinity of the interface (Fig. 4a) hint at the existence of mechanical growth stresses due to replacement of Fe with $FeCO_3$ or a precursory phase. These two aspects are discussed in more detail in chapter 3.3.1.

The STEM EDX elemental mapping (Fig. 4b) shows that chloride is homogeneously present in the IL, at least within 500 nm from the interface. Concentrations of up to 5 at.% are found and it is not associated with sodium, which would suggest a pore space precipitate formed after sample extraction from the experiment. The HRTEM-BF image (Fig. 4c) shows a crystalline phase approx. 50 nm from the interface. The orientation of the crystal towards the electron beam could not be identified, but obviously a low indexed zone axis is parallel to the electron beam. The lattice spacing within the crystalline region is measured to ~0.76 nm in two directions, with an included angle of ~90°. However, the largest possible lattice spacing for $FeCO_3$ is significantly lower at 0.36 nm. Additionally, it was observed that the interaction with the electron beam altered the sample as visible from changes of the lattice and the calculated Fast Fourier transforms (FFT) that resemble a diffraction pattern (comparison between Fig. 4c left and right).

3.2.2. 160 °C and 240 °C corrosion films

SEM images of 160 °C and 240 °C samples after 1 day of corrosion show crystalline $FeCO_3$ forming an OL (Fig. 5a, b). The $FeCO_3$ crystals reach sizes of up to 20 µm at 160 °C and up to 50 µm at 240 °C. As in the case for 80 °C, the $FeCO_3$ crystals have the morphology of a precipitate that grows outwards without confinement. The degree of coverage with $FeCO_3$ crystals after 1 day of exposure has been estimated to be ~60 % at 160 °C and ~90 % at 240 °C, reflecting the higher corrosion rate at 240 °C. In fact, at any given time the degree of coverage is higher at 240 °C. The number of $FeCO_3$ crystals per area increases with time until a coherent layer of $FeCO_3$ is formed after ~2 days at 240 °C and ~3 days at 160 °C, respectively. At this point there is a lateral growth confinement. XRD spectra (Fig. 5) have been measured on samples immersed for 1 day before a coherent $FeCO_3$ film is formed and minor phases are obscured. This is exemplified by the EDX map of Fe given in Fig. 5b. Higher Fe concentrations are measured where no $FeCO_3$ crystals cover the IL or the steel substrate.

The XRD spectrum for 240 °C (Fig. 5b) provides direct evidence of minor amounts of Fe-oxide, either Fe_2O_3 or mixed-valence Fe_3O_4. A further distinction cannot be made due to the low peak intensity, but similar studies often found Fe_2O_3 and Fe_3O_4 coexisting in a duplex film [25,28,29]. XRD spectra on 160 °C samples do not show any Fe-oxide. This seems thermodynamically implausible and not in accordance with other studies conducted under similar conditions. We therefore assume that the diffraction signal for Fe-oxide is too weak due to its relatively low volume fraction within the film.

A TEM analysis was performed on the corrosion film formed at 160 °C. Fig. 6a gives an overview of the lamella. Three different regions have been labeled (Fig. 6b): (i) Internal oxide (IO) describes a region where a localized corrosion feature allows the Fe-oxide film to grow to higher thickness (~1 µm). (ii) The intermediate region shows a relatively smooth part of the substrate covered with a Fe-oxide film that has a thickness of ~25 nm. (iii) Siderite/external oxide is where a µm-sized $FeCO_3$ crystal sits on the surface.

As anticipated, element mapping in the intermediate region (ii) exhibits mainly Fe and O in the film (Fig. 6c), which confirms the presence of a coherent film of Fe-oxide. The high-resolution TEM images in Fig. 6d show that the Fe-oxide film is polycrystalline with crystal sizes on the order of a few nm. Lattice fringes can be observed, indicating that the crystals have grown with random orientation. Even

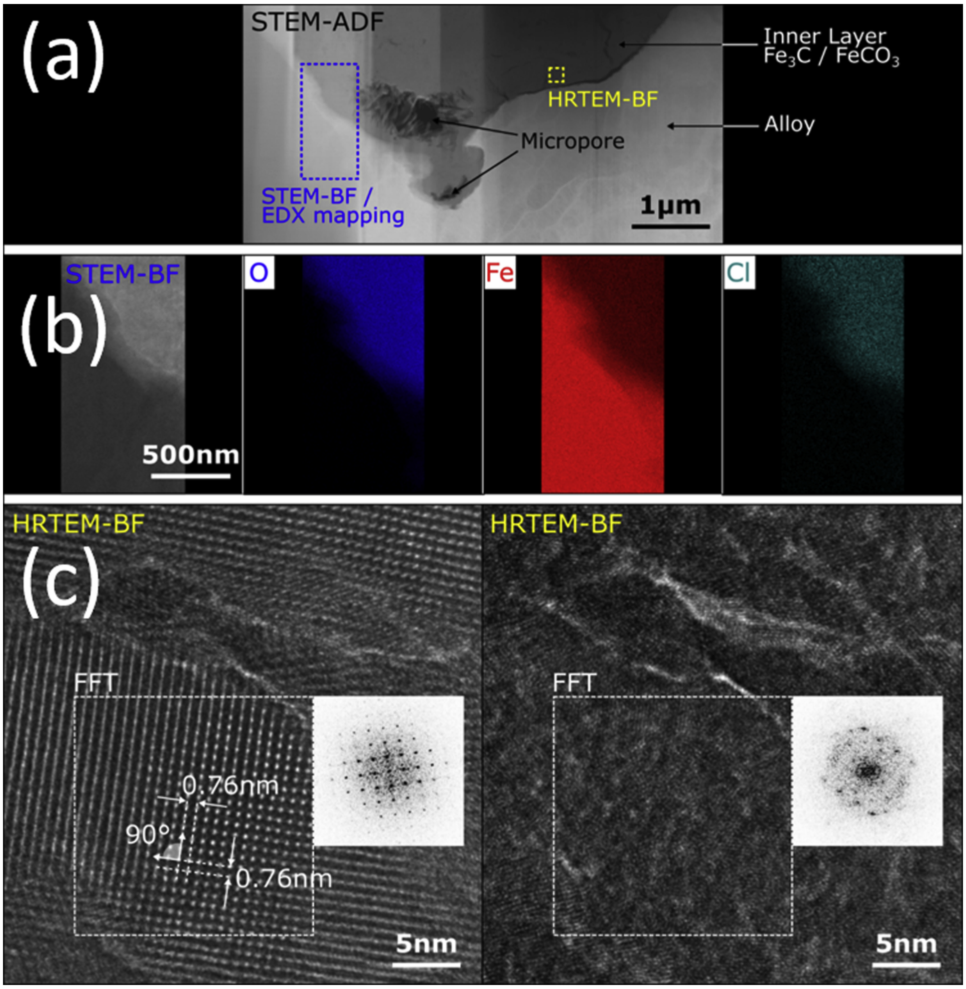

Fig. 4. (a) STEM-ADF image of the FIB lamella (cross-section); (b) STEM-BF image and quantitative element mappings of O, Fe and Cl over the metal/IL interface. (c) High-resolution TEM images of the IL at the same site. The interaction with the electron beam alters the sample as visible from changes of the lattice and the calculated fast Fourier transforms that resemble a diffraction pattern.

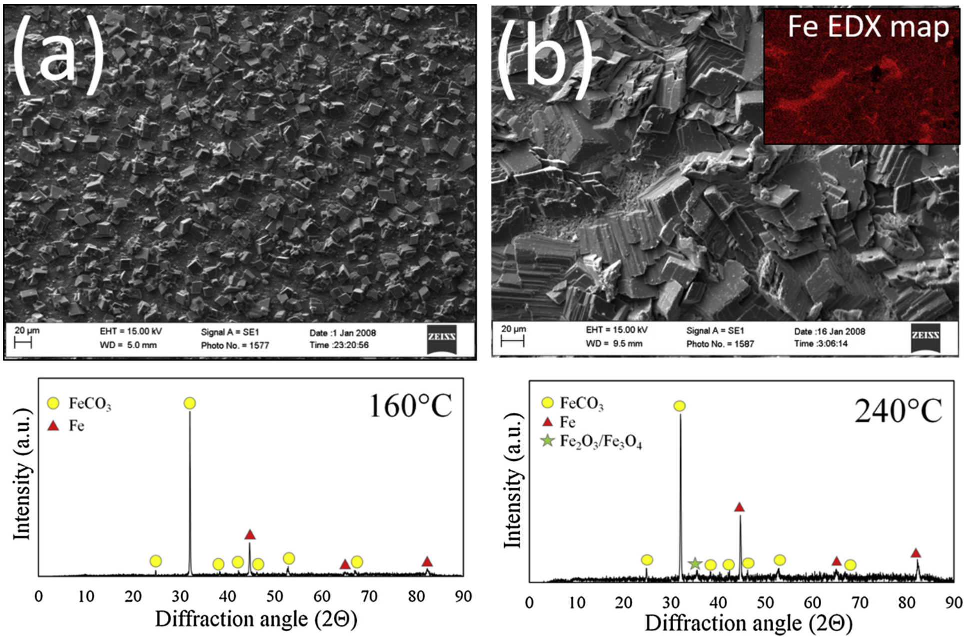

Fig. 5. Top view SEM pictures of corrosion films formed after 1 day: (a) 160 °C and (b) 240 °C; Fig. 4b also gives an EDX map of Fe of the same area as the SEM image; XRD spectra for 160 °C and 240 °C for the same samples are given below the SEM images.

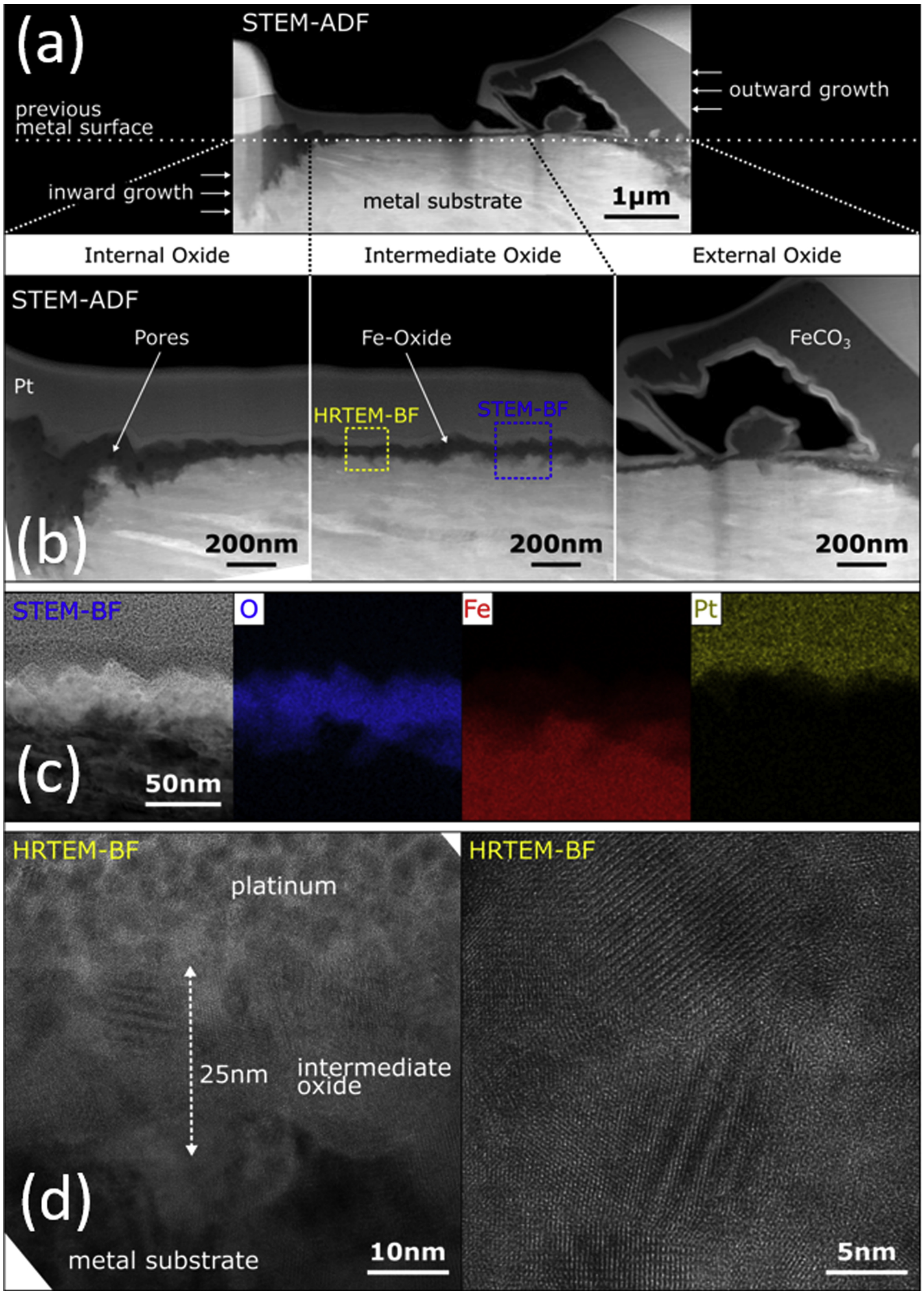

Fig. 6. (a) STEM-ADF image of the FIB lamella (cross-section); (b) details of the regions displaying an internal oxide, an intermediate oxide and an external oxide; (c) STEM-BF image and quantitative element mappings of O, Fe and Pt at the intermediate oxide region. (d) High-resolution TEM images of the metal/oxide film interface.

close to the steel substrate, the Fe-oxide is crystalline. In some areas, the Fe-oxide film appears to contain significant porosity on the nanoscale, particularly where we observed localized corrosion features and below $FeCO_3$ crystals (Fig. 6b).

Regarding the protective properties of the corrosion film, we can conclude that under the experimental conditions, Fe-oxide is more effective in lowering the corrosion rate than $FeCO_3$. It typically does not form thick crystalline films and nucleation occurs on very short time scales [30]. Nearly instantaneous formation of Fe-oxide prevents Fe_3C-catalyzed corrosion from occurring. $FeCO_3$ forming on top of the Fe-oxide does not add substantial corrosion protection as evidenced by constant R_p values over the time scale in which a coherent $FeCO_3$ film forms (2–3 days).

3.3. Discussion of film-growth

As previously discussed, temperature was found to be a major factor in determining the properties of corrosion films. This mandates a discussion about the mechanism of film growth. As described in Shoesmith (1981), surface films typically form via two distinct mechanisms (1) a solid-state reaction and (2) a precipitation reaction [20]. Our results suggest that both mechanisms occur simultaneously leading to different outcomes at different temperatures.

3.3.1. 80 °C corrosion film

The bulk of the IL consists of $FeCO_3$, as evidenced by XRD and SEM-EDX. Its formation is facilitated by the presence of an undissolved Fe_3C

network (part of the former steel microstructure) that becomes successively impregnated with $FeCO_3$. Interestingly, micropores occur in locations where Fe_3C is absent (outline with red dotted line in Fig. 3a), which supports the hypothesis that Fe_3C facilitates $FeCO_3$ formation, or otherwise the pore space would be completely filled by $FeCO_3$. $FeCO_3$ is required to form in-situ without first dissolving into the electrolyte, or otherwise the Fe_3C network would likely be mechanically destabilized. The driving force for the oxidation reaction is the E_{corr} evolution (Fig. 2), which increases from -450 mV to -225 mV due to an enhancement of the cathodic reaction by subsequent exposure of electrochemically-active Fe_3C particles [31]. Exceeding the equilibrium potential for the redox reaction (e.g. $Fe + HCO_3^- \longrightarrow FeCO_3 + H^+ + 2e^-$) will therefore result in the formation of appreciable amounts of $FeCO_3$ (or its precursor phase) around the Fe_3C particles. However, as other studies have shown, significant overpotentials on the order of 50 mV are required to drive the electrochemical oxidation reaction [32]. This finding has been discussed in Mundhenk et al. and was attributed to the microstructure, particularly the C content, of the tested steel [12].

Regarding whether CO_2 corrosion films develop protective properties, Crolet et al. developed a theoretical framework where the formation of CO_2 corrosion films is explained by electrically conductive elements in the corrosion film [26]. Galvanic coupling between steel and Fe_3C can lead to $FeCO_3$ oversaturation a certain distance from the metal surface, thus creating unprotective films ("empty" Fe_3C adjacent to the steel surface). This mechanism appears to be of minor importance for our experiments since the IL appears to strongly adhere to the metal (Figs. 3a, 4 a). Galvanic coupling is therefore either absent or occurs only over a very short range creating $FeCO_3$ oversaturation very close to the steel surface. This requires $CO_{2(aq)}$ and/or HCO_3^-, being the active species in the pH region of $FeCO_3$ formation, to be transported to the metal surface, either through the pore network or by solid-state diffusion through the IL. Given the rate at which corrosion still occurs in the film-covered state only the first option is plausible. In fact, pores of different sizes within the IL can be seen in Figs. 3a and 4 a and are hypothesized to form a continuous electrolyte-filled network that allows film-forming reactants to reach the metal surface.

The absence of porosity along the M/IL interface suggests that the parent metal is almost entirely replaced by the corrosion product. However, due to the different molal volumes of Fe and the newly formed corrosion product not all of the released metal can be accommodated in the space vacated by the metal when it subsequently is included in the corrosion product. The M/IL interface is therefore inherently subject to a growth constraint and growth stresses may occur [28]. This scenario requires some of the metal cations to migrate outwards. It is believed that the OL is formed by metal cations migrating towards the electrolyte. Starting from the IL/OL interface, the OL grows epitaxially outwards as indicated by the red arrow in Fig. 3b. The volume ratio between IL and OL is approx. 1:6, suggesting that the formation of the OL occurs at a slower rate. At the same time dissolution of the OL might subsequently occur as evidenced by dissolution features on faceted $FeCO_3$ crystals.

Figs. 3a and 4 a show the M/IL interface from where the corrosion reaction occurs and from where the IL grows into the metal (as indicated by the red arrow in Fig. 3a). The TEM analysis challenges the common assertion that $FeCO_3$ is the primary corrosion product when Fe corrodes in the presence of CO_2. Instead, a crystalline phase is observed exhibiting a lattice spacing more than twice as large as the largest possible for $FeCO_3$ (0.76 nm vs. 0.36 nm), which incorporates ~5 at.% chloride and becomes instable when exposed to the electron beam. This indicates towards the formation of a precursory, potentially hydrated, phase that predates $FeCO_3$ formation. This is consistent with results by DeMarco et al. who described a sequence of phases (e.g. $Fe_2OH_2CO_3$ and $Fe_6OH_{12}CO_3$) in the early stages of corrosion that exhibit similar lattice spacings as observed in Fig. 4c [33]. From the XRD measurements, such phases are not visible since the respective high-intensity reflections would occur far below a 2θ of 15°. However, despite chloride being present in their experiments, DeMarco et al. do not report any chloride-containing phases [33]. In our 80 °C experiments chloride is largely present as cationic $FeCl^+$ and it is typically not known for participating in corrosion film-forming reactions. At this point we can only speculate as to what role chloride plays in the formation of the precursory corrosion product. Subsequently, the precursory phase eventually matures into $FeCO_3$, which we observe with XRD and SEM-EDX.

3.3.2. 160 and 240 °C corrosion film

The internal oxide (IO) layer grows at the metal-oxide interface by the access of a molecular oxidant (e.g. H_2O, H_2CO_3, HCO_3^-) through a network of pores as opposed to solid-state diffusion through the oxide which is much too slow to account for the observed growth rate. Our TEM results show a relatively compact Fe-oxide film in uniformly corroded areas (intermediate oxide). However, this does not prove the absence of nanopores. According to Robertson pores sizes of ~1 nm are sufficient to provide oxidant transport [29]. Significant porosity is observed in areas where, in the vicinity of localized corrosion features, the internal Fe-oxide grew to larger thickness (~1 μm; Fig. 6b). The spherical pores (Ø ≤ 40 nm) are likely the result of relatively fast film growth and deviate in their properties from the pores reported in Park & Macdonald for similar temperatures [27]. They described the formation of porous Fe-oxide films in which the pore space is located between relatively large agglomerated Fe-oxide crystallites (≤100 μm across). We hypothesize that these were formed by the Kirkendall effect, which describes the formation of pores during diffusion. Unequal diffusion rates between Fe cations and O anions produce voids that act as sinks for vacancies and eventually accumulate in an attempt to restore equilibrium.

3.4. Thermodynamic analysis of carbon steel corrosion

A thermodynamic analysis was conducted for carbon steel corrosion and corrosion film formation in CO_2-containing NaCl fluid up to 300 °C. We used both, PHREEQC and Geochemist's Workbench to thermodynamically model the electrochemical CO_2-NaCl-Fe-H_2O system and to compare with the experimental results.

Pristine natural geothermal fluids are typically strongly reducing in a geochemical sense, meaning that oxygen fugacity is very low. The redox state of the geothermal fluid not only determines the rate at which corrosion proceeds but also the stability of mineral phases that form as a consequence of corrosion. E_h values below $-50\ mV_{SHE}$ have been reported in different studies [5,34]. For corrosion experiments it is therefore crucial to keep the O_2 fugacity as low as possible. For the 80 °C and 160 °C we took effluent samples which contained measurable quantities of H_2 which shows that O_2 contamination is sufficiently low. The in-situ O_2 fugacity in our experiments was estimated in two different ways using EQ3/6 [35]. First, it was assumed to be fixed by the Fe^{3+}/Fe^{2+} couple, using the measured Fe concentration and equilibrium with magnetite. Second, it was assumed to be fixed by the water couple oxidation/reduction reaction, using the measured $H_2(g)$ concentration. The results were similar ($\log fO_2 = -49.2$ and -56.9, respectively), suggesting that reducing conditions prevailed at all temperatures.

For a thorough thermodynamic analysis of the CO_2-NaCl-Fe-H_2O system both, $[Fe^{2+}]$ and the pH have to be constrained. Both parameters can be assumed to be higher at the corroding interface than in the bulk solution. This local microenvironment develops due to the anodic reaction that produces Fe^{2+} cations and the cathodic HER. Typically, for the generation of Pourbaix diagrams the concentration of the dissolved species, here $[Fe^{2+}]$, is arbitrarily set to 1 μmol/l [36]. This assumption, however, is too low for an actively corroding system, where $[Fe^{2+}]$ in the bulk solution has been measured to be 50 μmol/l [12]. This value might even be higher locally, particularly when

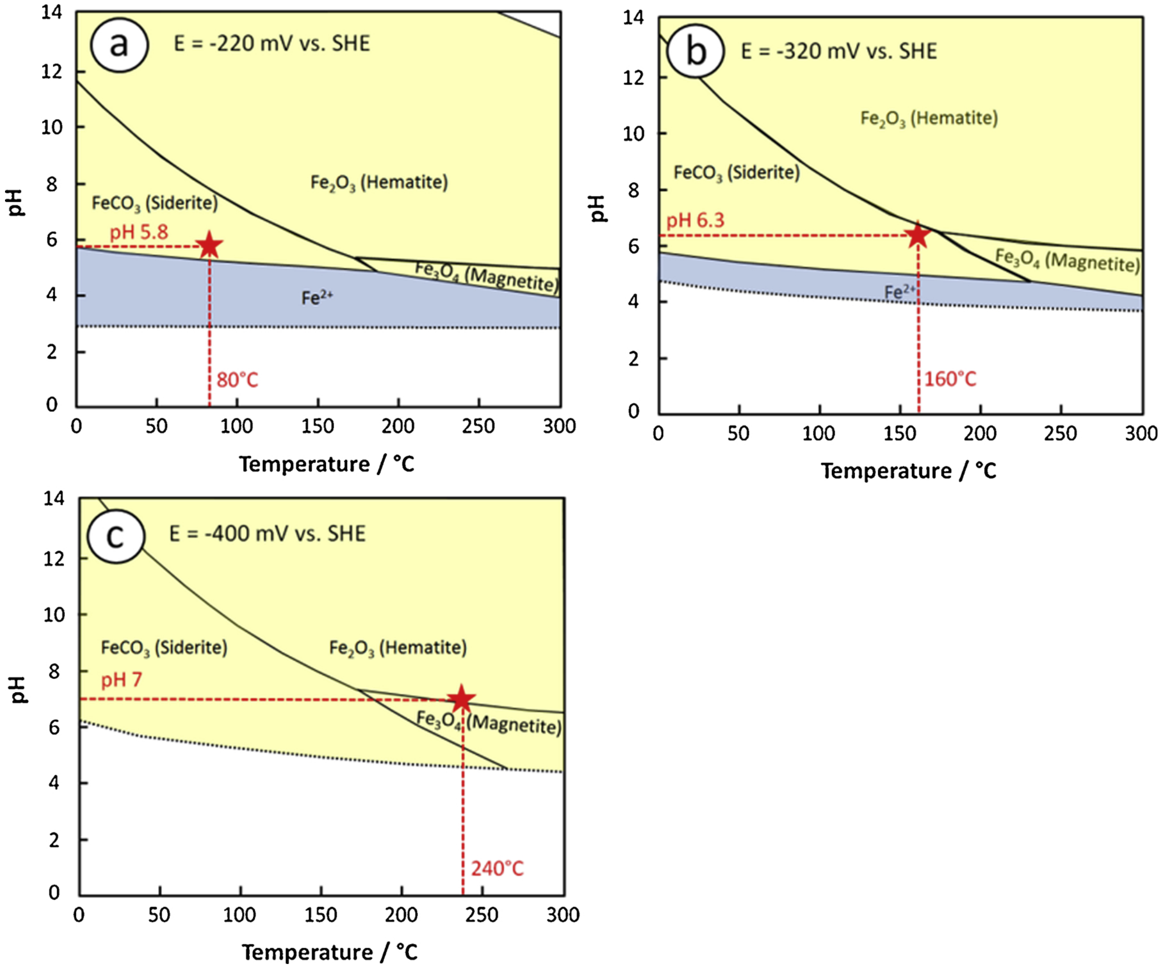

Fig. 7. Thermodynamic pH-temperature plots for three different electrochemical potentials: a: $-220\,mV_{SHE}$, b: $-320\,mV_{SHE}$, c: $-400\,mV_{SHE}$; Fe^{2+} concentration 50 µmol/l; 10 bar CO_2 partial pressure; the red asterisk marks the location of the corrosion system (temperature and estimated pH). (For interpretation of the references to colour in this figure legend, the reader is referred to the web version of this article.)

transport processes, e.g. in a porous film, are slow compared to the metal dissolution rate. Increasing $[Fe^{2+}]$ in the calculation generally shifts the boundary in favor of solid Fe phases, and vice versa.

Fig. 7 shows thermodynamic temperature-pH plots for different electrochemical potentials, reflecting the E_{corr} that we have measured for 80 °C, 160 °C, and 240 °C (Fig. 2). Based on other CO_2 corrosion studies we estimated the pH to be one unit higher than the bulk pH: 5.8 at 80 °C, 6.3 at 160 °C, and 7 at 240 °C, respectively [37,38]. The temperature-pH couple is indicated by a red asterisk in each of the plots. The plots reveal that with increasing temperature and lower electrochemical potentials Fe-oxide formation becomes thermodynamically favorable. Qualitatively, this trend is consistent with the results reported by Tanupabrungsun et al. who tested low-carbon steel in 1 wt.% NaCl solution with various partial pressures of CO_2 [21]. Based on thermodynamic calculations alone we would expect $FeCO_3$ at 80 °C, mixed oxide/$FeCO_3$ at 160 °C, and mixed oxide at 240 °C. In fact, this agrees well with other corrosion studies in this temperature range in which $FeCO_3$ disappears at a certain temperature, depending of the CO_2 partial pressure [39]. However, we observed $FeCO_3$ at all temperatures and resolve this apparent disagreement by accounting for the higher CO_2 partial pressure in our experiments which lead to the co-existence of Fe-oxide and $FeCO_3$. It has to be noted that the identity of the corrosion product is highly pH sensitive and that thermodynamic databases only contain thermodynamically stable phases.

4. Conclusions

Carbon steel corrosion was studied under geothermal conditions up to 240 °C in NaCl brine ($2\,mol\,kg^{-1}$) containing CO_2. Both, kinetic and thermodynamic aspects of high-temperature corrosion and associated corrosion film formation have been discussed. Several conclusions can be drawn from the study:

- Corrosion kinetics at 160 °C and 240 °C are relatively time-invariant, and almost one order of magnitude higher at 240 °C. In comparison, corrosion rates at 80 °C peak in the early stage of the experiments before a moderately protective corrosion film forms and R_p values exceed $1000\,\Omega\,cm^2$ after approx. 1 day.
- At 160 °C and 240 °C, continuous crystalline Fe-oxide films (thickness ~25 nm at 160 °C) form almost instantaneously and provide moderate corrosion protection. Subsequent formation of an outer $FeCO_3$ film provides no additional corrosion protection.
- Corrosion protection at 80 °C is achieved solely by a thick, but porous, duplex film. It continuously forms at the M/IL interface and grows inwards by replacing the ferrite component of the steel with $FeCO_3$ while the Fe_3C component from the original microstructure remains preserved.
- At 80 °C Fe-oxide is absent underneath the IL. Instead, TEM reveals a precursory, likely hydrated and chloride-containing, phase that predates $FeCO_3$ formation.
- Thermodynamic calculations show that towards higher

temperatures Fe-oxide is favored over $FeCO_3$ which is consistent with experimental results.

Data availability

The raw data required to reproduce these findings are available to download from Mundhenk, Niklas (2019), “Corrosion science publication”, Mendeley Data, V2, doi: 10.17632/tz69cynpny.2.

CRediT authorship contribution statement

N. Mundhenk: Conceptualization, Methodology, Investigation, Formal analysis, Writing - original draft, Writing - review & editing. **S. Carrero:** Visualization, Formal analysis. **K.G. Knauss:** Writing - review & editing, Formal analysis, Resources. **R. Wonneberger:** Visualization, Formal analysis, Writing - review & editing. **A. Undisz:** Visualization, Formal analysis, Writing - review & editing. **Y. Wu:** Conceptualization, Resources, Supervision.

Declaration of Competing Interest

The authors declare that they have no known competing financial interests or personal relationships that could have appeared to influence the work reported in this paper.

Acknowledgments

U.S. Department of Energy (DOE) funding was provided to the Hydrothermal Lab at Lawrence Berkeley National Laboratory under the Contract No. DE-AC02-05CH11231. Financial support by the German Research Foundation (DFG; Inst 275/391-1) is gratefully acknowledged.

References

[1] A.J. Ellis, W.A.J. Mahon, Chemistry and Geothermal System, Academic Press, New York, 1977.

[2] J. Banas, U. Lelek-Borkowska, B. Mazurkiewicz, W. Solarski, Effect of CO2 and H2S on the composition and stability of passive film on iron alloys in geothermal water, Electrochim. Acta 52 (2007) 5704.

[3] J. Scheiber, A. Seibt, J. Birner, N. Cuenot, A. Genter, W. Moeckes, Barite scale control at the Soultz-sous-Forets (France) EGS site, Proceedings 38th Workshop on Geothermal Reservoir Engineering Stanford University (2014).

[4] N. Mundhenk, P. Huttenloch, T. Kohl, H. Steger, R. Zorn, Metal corrosion in geothermal brine environments of the upper Rhine graben–laboratory and on-site studies, Geothermics 46 (2013) 14.

[5] N. Mundhenk, P. Huttenloch, B. Sanjuan, T. Kohl, H. Steger, R. Zorn, Corrosion and scaling as interrelated phenomena in an operating geothermal power plant, Corros. Sci. 70 (2013) 17.

[6] N. Mundhenk, P. Huttenloch, R. Bäßler, T. Kohl, H. Steger, R. Zorn, Electrochemical study of the corrosion of different alloys exposed to deaerated 80 °C geothermal brines containing CO2, Corros. Sci. 84 (2014) 180.

[7] S.N. Karlsdottir, K.R. Ragnarsdottir, A. Moller, I.O. Thorbjornsson, A. Einarsson, On-site erosion-corrosion testing in superheated geothermal steam, Geothermics 51 (2014) 170.

[8] M. Cabrini, S. Lorenzi, T. Pastore, M. Favilla, R. Perini, B. Tarquini, Material selection for dew-point corrosion in geothermal fluids containing acid chloride, Geothermics 69 (2017) 139.

[9] F.A. Posey, A.A. Palko, A.L. Bacarella, Corrosivity of Geothermal Brines, Progress Report Oak Ridge National Laboratory, 1977.

[10] Y. Kurata, N. Sanada, H. Nanjo, J. Ikeuchi, Casing pipe materials for deep geothermal wells, Geotherm. Resour. Counc. Trans. 19 (1995) 105–109.

[11] S. Nesic, Key issues related to modelling of internal corrosion of oil and gas pipelines–a review, Corros. Sci. 49 (2007) 4308.

[12] N. Mundhenk, K.G. Knauss, S.R.S. Bandaru, R. Wonneberger, T.M. Devine, Corrosion of carbon steel and the passivating properties of corrosion films formed under high-PT geothermal conditions, Sci. Total Environ. 677 (2019) 307.

[13] F. Farelas, M. Galicia, B. Brown, S. Nesic, H. Castaneda, Evolution of dissolution processes at the interface of carbon steel corroding in a CO2 environment studied by EIS, Corros. Sci. 52 (2010) 509.

[14] J. Han, S. Nesic, Y. Yang, B.N. Brown, Spontaneous passivation observations during scale formation on mild steel in CO2 brines, Electrochim. Acta 56 (2011) 5396.

[15] Z.F. Yin, W.Z. Zhao, Z.Q. Bai, Y.R. Feng, W.J. Zhou, Corrosion behavior of SM 80SS tube steel in stimulant solution containing H2S and CO2, Electrochim. Acta 53 (2008) 3690.

[16] B.R. Linter, G.T. Burstein, Reactions of pipeline steels in carbon dioxide solutions, Corros. Sci. 41 (1999) 117–139.

[17] R.F. Wright, E.R. Brand, M. Ziomek-Moroz, J.H. Tylczak, P.R. Ohodnicki, Effect of HCO3- on electrochemical kinetics of carbon steel corrosion in CO2-saturated brines, Electrochim. Acta 290 (2018) 626.

[18] G. Patzay, G. Stahl, F.H. Karman, E. Kalman, Modeling of scale formation and corrosion from geothermal water, Electrochim. Acta 43 (1998) 137.

[19] B. Ingham, M. Ko, N. Laycock, N.M. Kirby, D.E. Williams, First stages of siderite crystallization during CO2 corrosion of steel evaluated using in situ synchroton small- and wide-angle X-ray scattering, Faraday Discuss. 180 (2015) 171.

[20] D.W. Shoesmith, Formation, transformation and dissolution of phases formed on surfaces, Electrochemical Society Meeting, Ottawa, 1981.

[21] T. Tanupabrungsun, B. Brown, S. Nesic, Effect of pH on corrosion of mild steel at elevated temperatures, NACE Corros. 2348 (2013).

[22] D.L. Parkhurst, C.A.J. Appelo, User’s Guide to PHREEQC (Version 2): A Computer Program for the Speciation, Batch-Reaction, One-Dimensional Transport, and Inverse Geochemical Calculations; Water Resources Investigations Report 99–4259, U.S. Geological Survey, Reston, VA, 1999.

[23] C.M. Bethke, Geochemical Reaction Modeling: Concepts and Applications, Oxford University Press, New York, 1996.

[24] E. McCafferty, Validation of corrosion rates measured by the Tafel extrapolation method, Corros. Sci. 47 (2005) 3202.

[25] K.E. Heusler, B. Kusian, D. McPhail, Kinetics of the corrosion of iron in aqueous electrolytes at temperatures up to 300 °C, Ber. Bunsenges. Phys. Chem. 94 (1990) 1443.

[26] J.L. Crolet, N. Thevenot, S. Nesic, Role of conductive corrosion products in the protectiveness of corrosion layers, NACE Corros. 54 (1998) 194.

[27] J.R. Park, D.D. Macdonald, Impedance studies of the growth of porous magnetite films on carbon steel in high temperature aqueous systems, Corros. Sci. 23 (1983) 295–315.

[28] J. Robertson, The mechanism of high temperature aqueous corrosion of steel, Corros. Sci. 29 (1989) 1275–1291.

[29] M. Nagayama, M. Cohen, The anodic oxidation of iron in neutral solution I. The nature and composition of the passive film, J. Electrochem. Soc. 109 (1962) 781–790.

[30] T. Tanupabrungsun, D. Young, B. Brown, S. Nesic, Construction and verification of pourbaix diagrams for CO2 corrosion of mild steel valid up to 250 °C, NACE Corros. 1418 (2012).

[31] A. Dugstad, H. Hemmer, M. Seiersten, Effect of steel microstructure on corrosion rate and protective iron carbonate film formation, NACE Corros. 57 (2001) 369.

[32] G.A. Zhang, Y.F. Cheng, On the fundamentals of electrochemical corrosion of X65 steel in CO2-containing formation water in the presence of acetic acid in petroleum production, Corros. Sci. 51 (2009) 87.

[33] R. De Marco, Z.T. Jiang, B. Pejcic, E. Poinen, An in situ synchroton radiation grazing incidence X-ray diffraction study of carbon dioxide corrosion, J. Electrochem. Soc. 152 (2005) 389–392.

[34] C. Wanner, F. Eichinger, T. Jahrfeld, L.W. Diamond, Causes of abundant calcite scaling in geothermal wells in the Bavarian Molasse Basin, Southern Germany, Geothermics 70 (2017) 324.

[35] T.J. Wolery, K.J. Jackson, W.L. Bourcier, C.J. Bruton, B.E. Viani, K.G. Knauss, J.M. Delany, The EQ3/6 software package for geochemical modeling: current status, Amer. Chem. Soc. Symposium Series, in: D.C. Melchior, R.I. Bassett (Eds.), Chemical Modeling in Aqueous Systems II, 416 1990, p. 104.

[36] D. Landolt, Corrosion and Surface Chemistry of Metals, EPFL Press, Lausanne, 2007.

[37] Td.C. Almeida, M.C.E. Bandeira, R.M. Moreira, O.R. Mattos, New insights on the role of CO2 in the mechanism of carbon steel corrosion, Corros. Sci. 120 (2017) 239–250.

[38] R. De Motte, R. Mingant, J. Kittel, F. Ropital, P. Combrade, S. Necib, V. Deydier, D. Crusset, Near surface pH measurements in aqueous CO2 corrosion, Electrochim. Acta 290 (2018) 605–615.

[39] Y. Hua, S. Xu, Y. Wang, W. Taleb, J. Sun, L. Zhang, R. Barker, A. Neville, The formation of FeCO3 and Fe3O4 on carbon steel and their protective capabilities against CO2 corrosion at elevated temperature and pressure, Corros. Sci. 157 (2019) 392.